



ACADEMIC
PRESS

Available online at www.sciencedirect.com

SCIENCE @ DIRECT®

Journal of Sound and Vibration 266 (2003) 119–146

JOURNAL OF
SOUND AND
VIBRATION

www.elsevier.com/locate/jsvi

Direct computation of the noise radiated by a subsonic cavity flow and application of integral methods

X. Gloerfelt*, C. Bailly, D. Juvé

LMFA, UMR CNRS 5509, Ecole Centrale de Lyon, 69134 Ecully, France

Received 15 May 2002; accepted 6 September 2002

Abstract

The goal of this paper is to investigate the acoustic field generated by the flow over a cavity using two different and complementary numerical methods. First, a Direct Numerical Simulation of the 2-D compressible Navier–Stokes equations is performed to obtain directly the radiated noise. The results of the acoustic and aerodynamic fields are compared to the experimental data in the literature. Second, this reference solution is compared to solutions provided by hybrid methods using the flowfield computed inside the cavity combined with an integral formulation to evaluate the far-field noise. Numerical issues of three integral methods are studied: the Ffowcs Williams and Hawkins analogy that extends Lighthill's theory to account for solid boundaries and two Wave Extrapolation Methods from a control surface, the Kirchhoff and porous Ffowcs Williams and Hawkins methods. All methods show a good agreement with the Direct Numerical Simulation, but the first one is more expensive owing to an additional volume integral. However, the analogy can help in the analysis of wave patterns, by separating the direct waves from the reflected ones. The wave extrapolation methods from a surface are more efficient and provide a complementary tool to extend Computational Aeroacoustics near field to the very far field.

© 2002 Elsevier Ltd. All rights reserved.

1. Introduction

Impinging shear layers are known to exhibit strong coherent oscillations associated with intense noise radiation in a wide range of applications [1]. In this study, the noise radiated by a subsonic flow past a two-dimensional cavity is investigated. A severe acoustic environment within and

*Corresponding author. Xavier Gloerfelt, Centre Acoustique, Ecole Centrale de Lyon, 69134 Ecully France. Tel.: 33-4-72-18-60-12; fax: 33-4-72-18-91-43.

E-mail address: xavier.gloerfelt@ec-lyon.fr (X. Gloerfelt).

outside the cavity arises from a feedback loop, locked in by the geometry and the flow itself, as shown by many experimental observations [2]. However, geometrical simplicity does not imply a simple self-sustained mechanism, and numerous phenomena are involved. The direct calculation of the aerodynamic field and the acoustic field in the same computation by solving the compressible Navier–Stokes equations provides a new tool to investigate how the deformation of flow structures, their interactions with the downstream edge, the dynamics of the separated shear layer, the internal recirculating flow or the changes of flow regime with changing geometry and flow parameters are related to the intense radiated noise.

The direct simulation of aerodynamic noise remains a difficult numerical challenge, and only basic configurations with moderate Reynolds number flows can be treated with success [3]. Owing to the great disparities between fluctuations in the flow and in the sound field, specific numerical techniques must be used such as high order explicit schemes, minimizing dispersion and dissipation of acoustic waves, and appropriate boundary conditions. The term CAA (computational aeroacoustics) is therefore used. In conventional computational fluid dynamics (CFD) acoustics is either not resolved or not resolved accurately because of the numerical schemes used and inadequate grid cell sizes or time steps.

Approaches specific to aeroacoustics have been developed when the direct calculation of noise is proscribed. This group of approaches separates the aerodynamic calculation and the noise propagation problem in order to apply at each step the most appropriate method. One of the first theories on aerodynamic noise generation was established by Lighthill [4]. It was extended by Ffowcs Williams and Hawkings [5] (FW–H) to take into account the presence of solid boundaries in arbitrary motion. These integral formulations can be used in connection with numerical simulations of the Navier–Stokes equations to evaluate noise radiation. Another class of integral methods rests upon the Kirchhoff–Helmholtz theorem. The most famous one is the Kirchhoff method, extended by Farassat and Myers [6] for moving surfaces. The use of the FW–H formulation on a fictitious porous surface was proposed as an alternative solution in the original paper of Ffowcs Williams and Hawkings [5]. These Wave Extrapolation Methods (WEM) from a control surface, like Kirchhoff’s or porous FW–H methods, assume that the surface encloses all non-linear sources. All these integral formulations have similar analytical features based on a Green function formalism and suffer from the limitation of the observer in a uniform flow. The linear wave equation is assumed valid outside the source region, and consequently non-linear propagation of acoustic waves is not described.

The aim of this paper is to study three integral formulations: the Ffowcs Williams and Hawkings analogy, and two WEMs from a surface, the Kirchhoff and the FW–H WEM methods, and to evaluate their practical interest and complementarity. In particular, for the case of cavity flow it is shown how these different tools can help one to analyze the radiated acoustic field. The first part of this paper presents the direct computation of the Navier–Stokes equations for a two-dimensional rectangular cavity with aspect ratio of 2, matching one configuration of Karamcheti’s experiments [7]. In the second part, the far-field noise, associated with sources computed from the previous direct numerical simulation (DNS), is obtained using the three integral formulations. Each method is described and the results are compared with those of direct acoustic simulation taken as a reference.

2. Direct computation of cavity noise

2.1. Introduction

As in jet noise simulation, initial attempts have been made in the case of supersonic flows for cavity noise. These first CFD computations of compressible cavity flows used the 2-D unsteady RANS (Reynolds Averaged Navier–Stokes) equations with a turbulence model [8]. The effectiveness of such models for separated flows remains an open question. Slimon et al. [9] have found that RANS simulations show a strong sensitivity to the choice of turbulence models. Tam et al. [10] showed that the results are affected by high values taken by the turbulent viscosity. They even noticed better results for the estimation of the time-averaged surface pressure field with no model. That is why Rona and Dieudonné [11] preferred to study laminar flow motion. The absence of an eddy viscosity and a second order algorithm give a moderate dispersion and dissipation. However, this choice, as well as the one of a relaxation length, is often made on an ad hoc basis. To compute the broadband nature of cavity noise at high Reynolds numbers, it is important to take account of the turbulent mixing. Zhang [12] developed an approach coupling the unsteady RANS equations and a k - ω model including compressibility corrections. But all these applications were performed with supersonic flows, simplifying the problem.

The first computations of acoustic radiation from a cavity with a subsonic grazing flow have been carried out recently by Colonius et al. [13] and Shieh and Morris [14] using 2-D DNS at a Reynolds number based on cavity depth $Re_D \simeq 5000$. These simulations show a transition to a new flow regime when the ratio L/δ_θ of the cavity length over the momentum thickness becomes large. This mode is characterized by the shedding of a single vortex which occupies all the cavity. The periodic ejection of this structure is associated with an increase of the cavity drag. A similar transition was noted in the experiments of Gharib and Roshko [15] in a water tunnel. The new regime was called a wake mode because of the drag increase. However, the presence of the wake mode has not been seen in experiments of compressible cavity flows at subsonic speeds, for these aspect ratios. The same numerical bifurcation has also been noted by the authors [16]. To investigate higher Reynolds numbers ($Re_D \simeq 2 \times 10^5$), Shieh and Morris [17] applied CAA tools to solve unsteady RANS with a turbulence model: the one equation Spalart–Allmaras turbulence model and Detached Eddy Simulation have been implemented. The transition to a wake mode is still observed, demonstrating that it is related to the 2-D constraint rather than to the Reynolds number. When the cavity length is large compared to the thickness of the incoming boundary layer, Najm and Ghoniem [18] show in the same manner that the recirculation zone takes the form of a large-scale eddy that breaks away and migrates downstream, overshadowing the role of the usual smaller-scale vortices. However, this too strong recirculating flow is fed by the 2-D inverse cascade of energy. Vortex stretching, necessarily 3-D, should modify significantly the turbulent mixing between the clipped part of the shear layer and the corresponding counter-rotating vortex produced by the conservation of vorticity at the downstream edge. This turbulent mixing would prevent untimely transition to wake mode. In the present 2-D simulation, a short aspect ratio and a relative thick incoming boundary layer are chosen to ensure the shear layer mode of oscillations.

One configuration of Karamcheti's experiments [7] is reproduced numerically with the same dimensions as in the experiment. Karamcheti studied the acoustic radiation from 2-D rectangular cavities cut into a flat surface at low Reynolds numbers. The acoustic fields were investigated by

means of schlieren observations, interferometry, and use of a hot-wire anemometer. The measurement used a cutout spanning the 4×10 inch transonic wind tunnel and ending by a moving plate to obtain cavities of various length L , the depth D being the same for all of them, fixed at 0.1 inch. The case retained is a length-to-depth ratio of 2 ($L = 5.18$ mm and $D = 2.54$ mm); the boundary layer ahead of the cavity is laminar, and the freestream Mach number is 0.7. The Reynolds number based on cavity depth is $Re_D = 41\,000$. The choice of a high subsonic speed is interesting because the frequency increases slightly with Mach number, and the cavity is no longer compact relative to the acoustic wavelength. Moreover, the test case is more relevant for integral methods because mean flow effects on sound propagation become important.

2.2. Numerical methods

2.2.1. Governing equations

A DNS (no turbulence model) of the 2-D compressible Navier–Stokes equations is performed. The conservative form of these equations in a Cartesian co-ordinate system can be written as

$$\frac{\partial \mathbf{U}}{\partial t} + \frac{\partial \mathbf{E}_e}{\partial x_1} + \frac{\partial \mathbf{F}_e}{\partial x_2} - \frac{\partial \mathbf{E}_v}{\partial x_1} - \frac{\partial \mathbf{F}_v}{\partial x_2} = 0,$$

where

$$\begin{aligned} \mathbf{U} &= (\rho, \rho u_1, \rho u_2, \rho e)^t, & \mathbf{E}_e &= (\rho u_1, p + \rho u_1^2, \rho u_1 u_2, \rho u_1 h)^t, \\ \mathbf{F}_e &= (\rho u_2, \rho u_2 u_1, p + \rho u_2^2, \rho u_2 h)^t, & \mathbf{E}_v &= (0, \tau_{11}, \tau_{12}, u_1 \tau_{11} + u_2 \tau_{12} - q_1)^t, \\ \mathbf{F}_v &= (0, \tau_{21}, \tau_{22}, u_1 \tau_{21} + u_2 \tau_{22} - q_2)^t. \end{aligned}$$

The quantities ρ , p , u_i are the density, pressure, and velocity components, while e and h are the total energy and total enthalpy per mass unit. For a perfect gas,

$$e = p/[(\gamma - 1)\rho] + (u_1^2 + u_2^2)/2, \quad h = e + p/\rho, \quad p = r\rho T,$$

where T is the temperature, r the gas constant, and γ the ratio of specific heats. The viscous stress tensor τ_{ij} is modelled as a Newtonian fluid and the heat flux component q_i models thermal conduction in the flow with Fourier's law, thus

$$\tau_{ij} = \mu \left(\frac{\partial u_i}{\partial x_j} + \frac{\partial u_j}{\partial x_i} - \frac{2}{3} \delta_{ij} \frac{\partial u_k}{\partial x_k} \right), \quad q_i = -\frac{\mu c_p}{\sigma} \frac{\partial T}{\partial x_i}$$

where μ is the dynamic molecular viscosity, σ the Prandtl number, and c_p the specific heat at constant pressure.

2.2.2. Algorithm

When the above equations are solved numerically, it is imperative that neither the amplitude nor the propagation speed of acoustic waves be altered by the numerical scheme. Following the work of Bogey [19], high order algorithms are implemented. The equations are advanced in time using an explicit fourth order Runge–Kutta scheme, and the Dispersion–Relation Preserving scheme developed by Tam and Webb [20] is used to obtain spatial derivatives. A selective damping has also to be introduced in order to filter out non-physical short waves resulting from the use of finite differences and/or the treatment of boundary conditions.

2.2.3. Boundary treatment

This is the second key point of an aeroacoustic simulation. Non-reflecting conditions are required to avoid spurious reflections that can superpose onto the physical waves. To this end, the radiation boundary conditions of Tam and Dong [21], using a polar asymptotic solution of the linearized Euler equations in the acoustic far field, are applied to the inflow and to the upper boundaries. At the outlet, the outflow boundary conditions of Tam and Dong, where the asymptotic solution is modified to allow the exit of vortical and entropic disturbances, is combined with a sponge zone to dissipate vortical structures in the region where the shear layer leaves the computational domain. This sponge zone, represented in Fig. 1, is obtained by making use of grid stretching and progressive additional damping terms. Bogey et al. [22] have shown its efficiency in situations where large amplitude non-linear disturbances must exit the domain without significant numerical reflections.

Along the solid walls, the reflection method is applied by using three rows of fictitious points outside the computational domain. The fictitious values are defined by antisymmetric reflection of u_1 and u_2 , and symmetric reflection of p and ρ . The no-slip condition $u_1 = u_2 = 0$ is superimposed, and the wall temperature T_w is calculated using the adiabatic condition. This formulation ensures sufficient robustness by keeping centred differencing at the wall. It leads however to an overspecification of the variables at the wall, and can generate spurious high-frequency waves which are eliminated by artificial damping.

2.2.4. Numerical specifications

The computational mesh displayed in Fig. 1, is built up from a non-uniform Cartesian grid with 147×161 points inside the cavity and 501×440 outside, highly clustered near the walls. The minimum step size corresponds to $\Delta y_{min}^+ = 0.8$ in order to resolve viscous scales near the wall. The computational domain extends over $8.5D$ vertically and $12D$ horizontally to include a portion of the radiated field. The upstream and downstream boundaries are sufficiently far away from the

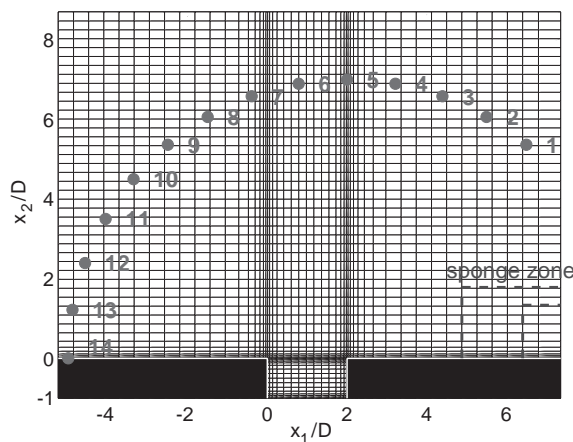


Fig. 1. Computational grid for cavity $L/D = 2$ (shown every other ten points). ●, data sampling locations for directivity evaluation; ---, refers to the location of the progressive additional sponge zone.

cavity to avoid possible self-forcing. The spacing between two points reaches a value $\Delta y_{max} = 2.9 \times 10^{-5}$ m in the cavity and $\Delta y_{max} = 5.6 \times 10^{-5}$ m in the acoustic region.

The initial condition is a polynomial expression of the laminar Blasius boundary layer profile for a flow at Mach 0.7. This velocity profile found for the inflow is extrapolated into the entire computational domain, with an initial boundary layer thickness $\delta_0 \approx 0.2D$. A corrective term is added at the inflow during the computation to avoid a numerical drift of the expected inflow profile. The freestream air temperature T_∞ is 298.15 K and the static pressure p_∞ is taken as 1 atm.

The strongly anisotropic computational mesh induces a very stiff discretized system. For explicit time marching schemes, an extremely small time step has to be used in order to satisfy the stability CFL criterion: $\Delta t = 0.7 \times \Delta y_{min}/c_\infty = 6.06 \times 10^{-9}$ s. The mesh Reynolds number [20] of the selective damping is chosen as $Re_S = 4.5$. This artificial dissipation is applied a second time near the walls in order to damp the numerical oscillations arising at the intersection of cavity surfaces, which are singular points that cannot be described without ambiguity. It is equivalent to lowering the artificial dissipation process but, owing to the highly clustered grid used near the walls, it slightly affects the global accuracy of the simulation. The computation is 4 h long on a Nec SX-5, with a CPU time of 0.4 μ s per grid point and per iteration.

2.3. Results and discussion

2.3.1. Far-field results

Fig. 2(a) gives a monitored pressure history at $x_1/D = -0.04$ and $y_2/D = 2$ in the beginning of the acoustic region. The flow reaches a self-sustained oscillatory state after a time of about $25D/U_\infty$ but is still irregular until $65D/U_\infty$. During the first period, the natural cavity modes grow in amplitude and saturate. Then a transient period occurs during the time needed by the recirculating flow to become installed in the cavity.

The corresponding sound pressure level spectrum is depicted in Fig. 2(b). It displays one principal peak at $St = 0.66$, which corresponds to the periodic impingement of coherent structures at frequency f_0 . Several secondary peaks are observable at $St = 1.30$, 1.96 and 2.62 which correspond to the first $2f_0$, the second $3f_0$, and the third $4f_0$ harmonics. Most of the radiated noise energy is concentrated at the fundamental frequency and its first harmonics. A schlieren

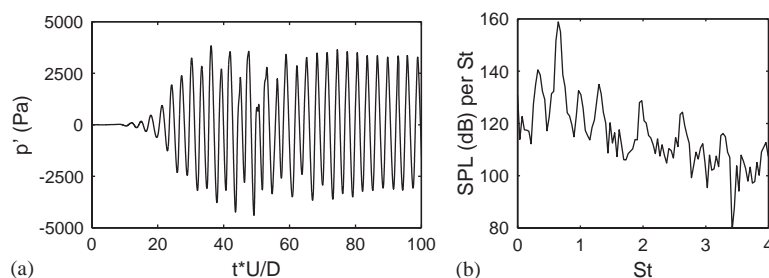


Fig. 2. Pressure history (a) versus non-dimensional time, and spectrum of pressure fluctuations (b) versus the Strouhal number $St = fL/U_\infty$, at $x_1/D = -0.04$ and $x_2/D = 2$. The spectrum is evaluated for tU/D between 50 and 100.

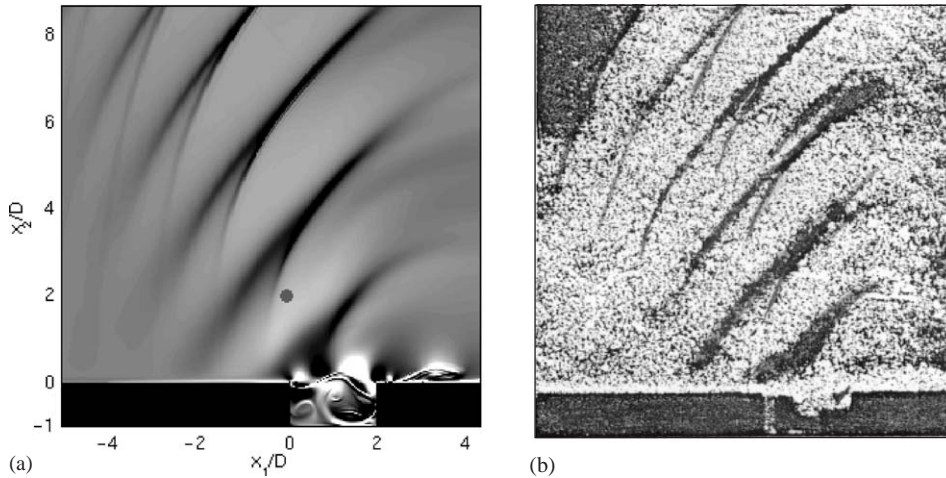


Fig. 3. Schlieren pictures corresponding to transversal derivative of the density: (a) present simulation, (b) Karamcheti's experiment [7]. The point in the left picture indicates the location of the pressure spectra calculation.

visualization, based on vertical gradients of density, shows the structure of the radiated field in Fig. 3(a). Two wave patterns are visible for the positive gradients (dark), which interfere during propagation. Their strong upstream directivity arises from the combined effects of the high-speed convection by the free stream and of the scattering due to the cavity walls. The scattering is mainly a combination of direct and reflected acoustic waves. These radiations are in qualitatively good agreement with the schlieren picture of Karamcheti (Fig. 3(b)). The experimental Strouhal number of the oscillations is $St = 0.69$, corresponding to an error of 5% in the frequency f_0 found in the present simulation. The 3-D effects or boundary layer characteristics may be responsible for this difference.

Karamcheti [7] estimated the intensity of acoustic radiation through interferometry. He found that the acoustic field could be very intense with values greater than 163 dB at a distance of $3D$ in the main propagation direction. These high-intensity levels are compatible with the present 2-D simulation, with a magnitude of sound pressure levels about 163.5 dB at $3D$, with an angle of 120° from the downstream.

2.3.2. Near-field results

The near field is now investigated to identify the noise generation mechanism, and in particular to determine the origin of the two waves patterns observed previously. Fig. 4 presents the vorticity field over one period of the well-established self-sustained oscillations. In Fig. 4(a), the shear layer is seen to reattach at the trailing edge and two vortical structures can be identified in the shear layer. The first one is just shed from the leading edge separation. This rolled-up vortex travels downstream in the next pictures, growing with convection. The second structure is located just upstream of the downstream edge. As it impinges on the edge (Fig. 4(b)), the incident vortex is clipped at its centre. Part of the vortex spills over the cavity and is convected downstream, increasing the thickness of the reattached boundary layer. The other component is swept downwards into the cavity creating recirculating regions (Fig. 4(c)). In Fig. 4(d), the vortex

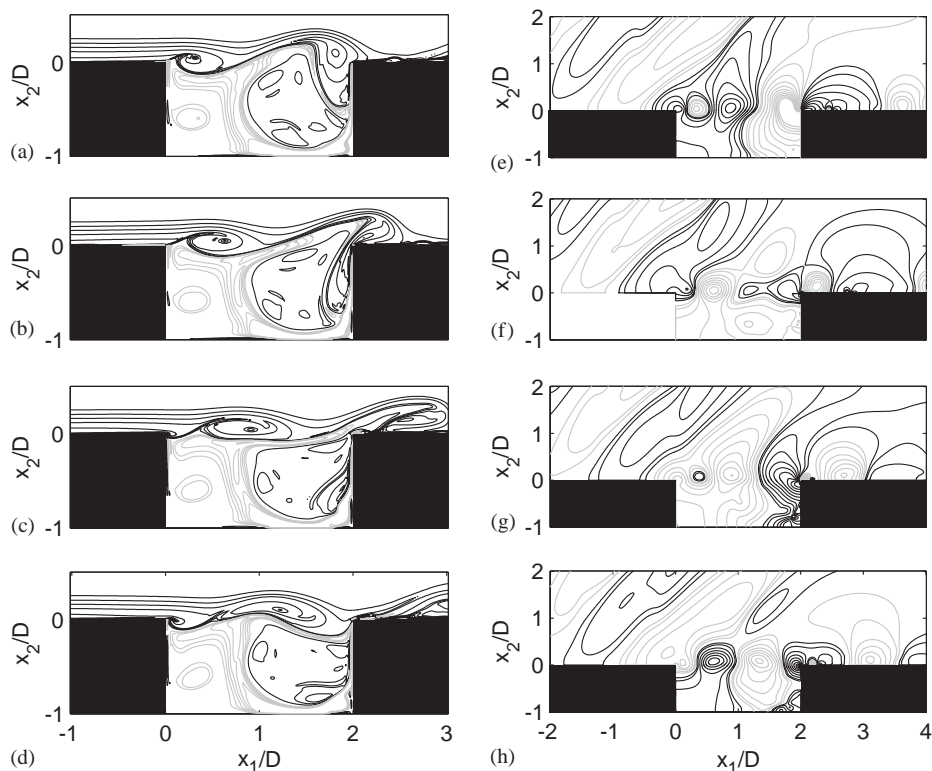


Fig. 4. Instantaneous vorticity contours (on the left) and pressure contours (on the right) at four times during one cycle. Sixteen contours between $\omega D/U_\infty = -10.5$ and 1.36 for vorticity and 22 contours between -10^4 and 10^4 Pa for pressure: —, negative contours: —, (in gray) positive contours. Zoom in and around the cavity.

generated at the leading edge in the first picture arrives at the trailing edge, sustaining the vortex impingement process.

The corresponding time-matched pressure field is depicted in Fig. 4, right column. It is not easy to identify the origins of the noise generation because three different patterns are superposed. The first one is associated with the two coherent structures evolving in the shear layer. Low-pressure regions in the shear layer identify vortices, separated by high-pressure regions. The two low-pressure centres are clearly visible in Fig. 4(h). The first one is associated with the vortex roll-up at the leading edge. The second one corresponds to the second vortex convected by the flow before it impinges the upstream edge. The second pressure pattern represents the recirculating flow in the cavity. As seen in the vorticity snapshots, a main recirculation zone is located in the second half of the cavity, associated with the low-pressure region inside the cavity, identifiable in Figs. 4(f) and (g). This large-scale region is not a single vortex but is actually made up of several smaller vortices, arising from the clipping process, and its central region is vorticity free. Lastly, the third group of pressure waves is the acoustic radiation generated by the flow. Fig. 4 shows the birth of a positive pressure wave in the impingement process. The previously generated wave, located at the leading edge in Fig. 4(e), escapes from the cavity in Fig. 4(h). In the latter picture, the pressure wave seems to result from the superposition of two acoustic radiations. It is still difficult to identify the two

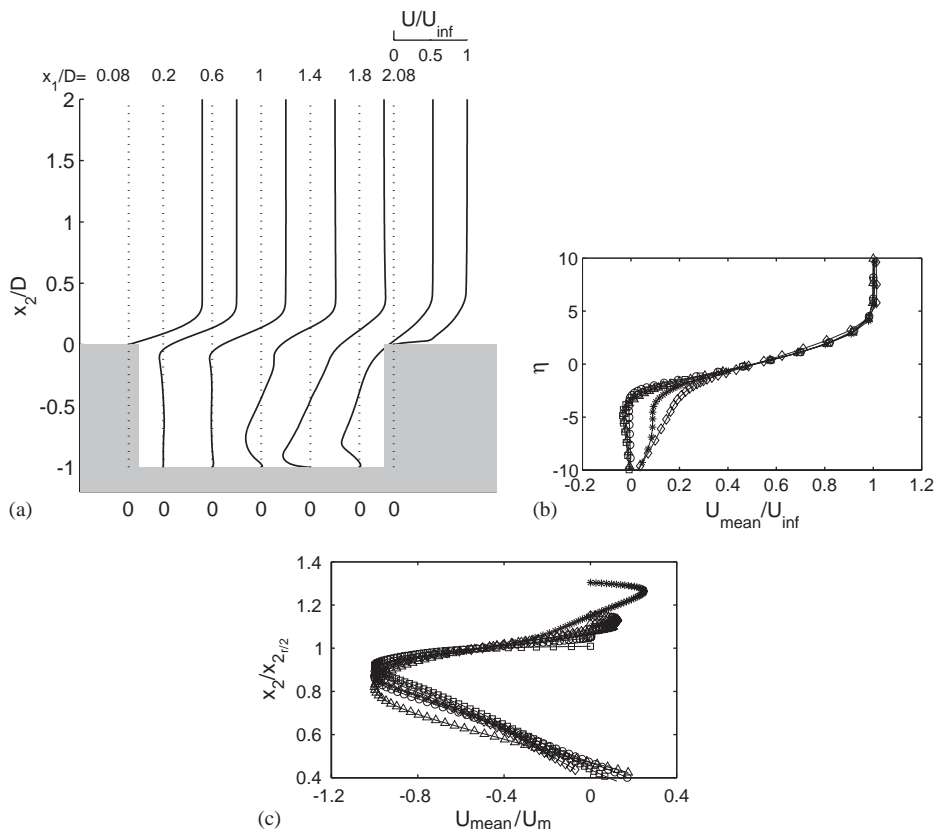


Fig. 5. Mean streamwise velocity profiles (a) and similarity of separated shear layer profiles at different longitudinal locations (b): \circ , $x_1/D = 0.05$; \square , $x_1/D = 0.22$; \triangle , $x_1/D = 0.56$; $*$, $x_1/D = 0.94$; \diamond , $x_1/D = 1.32$. Similarity in reverse flow velocity profiles at different longitudinal locations (c): \triangle , $x_1/D = 0.94$, \circ , $x_1/D = 1.13$; \square , $x_1/D = 1.51$; \diamond , $x_1/D = 1.82$; $*$, $x_1/D = 1.91$.

sources in the presence of interferences dominated by the aerodynamic pressure. This point will be discussed again in the next part.

2.3.3. Mean flow

The mean velocity profiles $\bar{u}_1(x_2)$ are shown in Fig. 5(a). In the early stages of the shear layer growth, the velocity changes from a boundary layer profile to a shear layer profile. Its momentum thickness is defined as

$$\delta_\theta = \int_{-\infty}^{+\infty} \frac{\rho \bar{u}_1}{\rho_\infty U_\infty} \left(1 - \frac{\rho \bar{u}_1}{\rho_\infty U_\infty} \right) dx_2$$

where $U_\infty = 242$ m/s and $\rho_\infty = 1.17$ kg/m³ are the velocity and the density of the free stream; the integration is performed between $\pm \delta$, where δ is the ordinate corresponding to $\bar{u}_1 = 0.99U_\infty$. At the leading edge, the boundary layer is laminar, and has a shape factor $H = \delta^*/\delta_\theta = 2.6$, where $\delta^* = 2.6 \times 10^{-4}$ m (displacement thickness), $\delta_\theta = 1.03 \times 10^{-4}$ m, the ratio $L/\delta_\theta = 49.3$, and the Reynolds number is $Re_{\delta_\theta} = 1661$. The shape factor is in good agreement with the value $H = 2.5$,

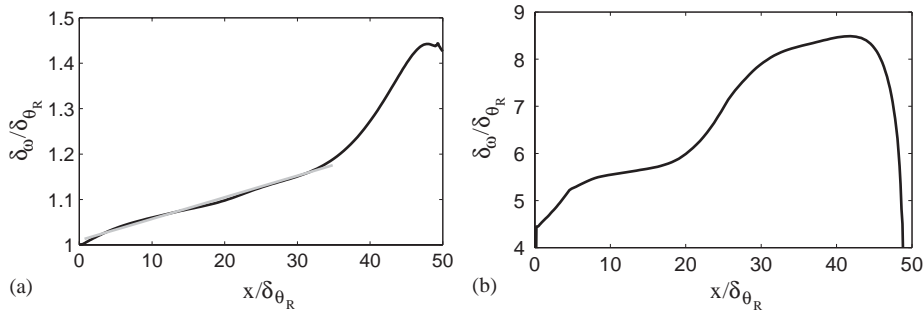


Fig. 6. Non-dimensional momentum thickness δ_θ (a), and non-dimensional vorticity thickness δ_ω (b), between the two corners of the cavity. δ_{θ_R} is the reference momentum thickness at the upstream edge.

reported by Sinha et al. [23] or Gharib and Roshko [15] for a laminar boundary layer ahead of the cavity. The growth of two characteristic thicknesses, the momentum thickness δ_θ , and the vorticity thickness δ_ω , defined as

$$\delta_\omega = U_\infty / |\partial \bar{u}_1 / \partial x_2|_{max}$$

are given in Fig. 6. As in the study of Forestier [24] for a transonic, $M = 0.8$, flow over a $L/D = 0.42$ cavity, and a Reynolds number $Re_L = 8.6 \times 10^5$, the growth is not linear but shows several stages. These shapes can be compared to the shear layer growth observed for forced mixing layers [25,26]. The rate of widening of δ_θ , in the first linear stage between $x_1/\delta_{\theta_R} = 0$ and 35, is 0.006 in good agreement with the value $d\delta_\theta/dx_1 \approx 0.006$, reported in measurements by Sarohia [27] for a $L/\delta_{\theta_R} = 52.5$ configuration.

A similarity is found when the mean velocity profiles are represented using the similarity parameter $\eta = (x_2 - x_{2_{0.5}})/\delta_\theta$, where $x_{2_{0.5}}$ corresponds to $\bar{u}_1 = 0.5U_\infty$ (Fig. 5(b)). In Fig. 5(a), strong deflections can be noted in the cavity and seem to be overestimated when compared to the experimental profiles obtained by Sinha et al. [23]. It comes undoubtedly from the too strong recirculation induced by the 2-D approach of the simulation. Nevertheless, the reverse flow in the cavity has qualitative features similar to those of a wall jet, observed by Sinha et al. [23] for laminar flow or by Lin and Rockwell [28] for turbulent cavity flows. Accordingly, these data are plotted in wall jet co-ordinates \bar{u}_1/U_m versus $x_{2,r/2}$ in Fig. 5(c), where U_m is the local maximum of the velocity \bar{u}_1 , and $x_{2,r/2}$ corresponds to $\bar{u}_1 = 0.5U_m$. The similarity is reached in the second half of the cavity. Considerable scatter still occurs near $x_2/x_{2,r/2} = 0.4$ and 1 but self-similarity for reverse flow is noticeable. Fig. 7 shows that the streamlines are closed in the cavity, displaying a large recirculation between the reverse flow and the shear layer.

2.3.4. Features of the shear layer

The intensity of fluctuations, defined as

$$u_{r.m.s.} = \sqrt{\overline{u_1^2}}/U_\infty, \quad v_{r.m.s.} = \sqrt{\overline{u_2^2}}/U_\infty, \quad w_{r.m.s.} = \sqrt{\overline{|u_1' u_2'|}}/U_\infty$$

are plotted in Fig. 8(a) and (b). The $u_{r.m.s.}$ profiles show the rapid appearance of a double peak in the distributions. For a forced shear layer [26], or for cavities with a large ratio L/δ_θ [24,29], the double peak appears progressively. The present distributions can be compared to those obtained

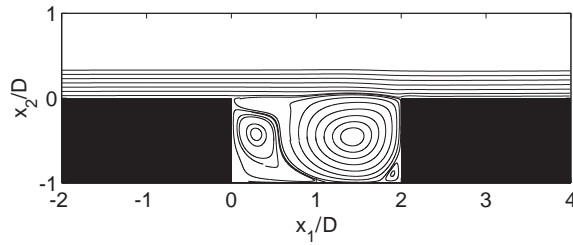


Fig. 7. Streamlines of the cavity flow.

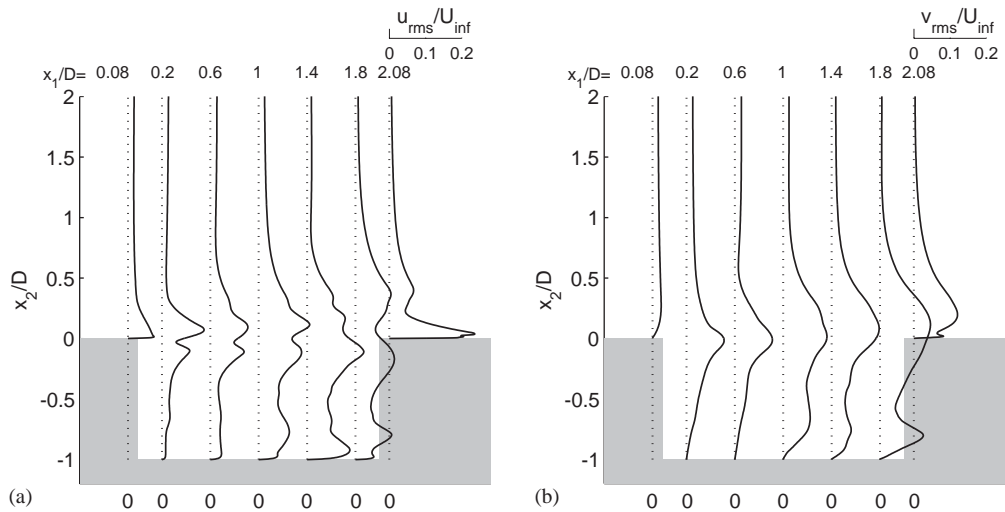


Fig. 8. Horizontal velocity fluctuations $u_{r.m.s.}$ (a) and vertical velocity fluctuations $v_{r.m.s.}$ (b) at different x_1 locations.

by Ziada and Rockwell [30] for the interaction between a shear layer and a wedge. This is characteristic of the presence of well-aligned vortices in the shear layer due to the resonant vortex shedding. The widening of the distributions corresponds to the slight growth of vortices with advection. The profiles are considerably affected by the recirculation zone inside the cavity, especially for large x_1/D , where the wall jet characteristics overshadow the shear layer behaviour. The scatter observed on the outside edge of the shear layer can be related to the presence of strong acoustic disturbances in the near field of the downstream corner. The level of the velocity fluctuations, as high as 0.16, is consistent with previous experimental results by Sarohia [27] for laminar flow. The vertical velocity fluctuations show a bell-shaped distribution all along the shear layer (Fig. 9(b)). The vertical intensities are of the same order as the horizontal ones, $v_{r.m.s.} = 0.14$. The experiments of Oster and Wygnanski [26], for forced mixing layers, underline a reinforcement of the vertical component and a decrease of intensities in the spanwise direction, in comparison with the unperturbed flow. This suggests a bidimensionalization of the flow, which explains why the vertical intensities are not overestimated in the present 2-D simulation. The maximum shear stress $uv_{r.m.s.}$ reaches a magnitude of 0.013. Kistler and Tan [31] report a value of 0.012 for a quasi 2-D cavity shear layer, and Gharib and Roskho [15] find the value 0.013.

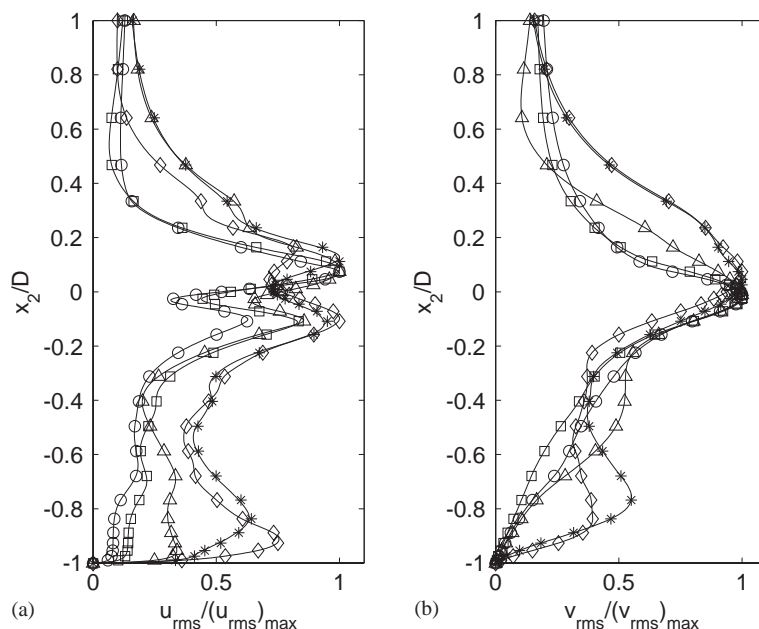


Fig. 9. Horizontal normalized velocity fluctuations $u_{r.m.s.}$ (a) and vertical normalized velocity fluctuations $v_{r.m.s.}$ (b). \circ , $x_1/D = 0.18$; \square , $x_1/D = 0.32$; \triangle , $x_1/D = 0.70$; $*$, $x_1/D = 1.08$; \diamond , $x_1/D = 1.27$.

To summarize, the characteristics of the shear layer agree with measurements and depict the behaviour of an excited shear layer. The Strouhal number based on the momentum thickness is $St_\theta = 0.014$, near the value 0.017 for the most unstable frequency of a hyperbolic-tangent velocity profile in the linear stability analysis. The initial vortex-formation frequency f_r is seen to match the forcing frequency f_0 . The level of the fundamental f_0 suppresses the growth of the subharmonic $f_0/2$, and vortex pairing is delayed. A row of vortices is generated and interacts with the downstream edge. The absence of pairing events explains the weak growth rate of the shear layer, only marked by the vortex passage and by the viscous growth of the convected vortical structures.

2.3.5. The global feedback in the cavity

A distinguishing feature of the self-sustained oscillations considered here is the existence of a feedback loop involving the excitation of instabilities in the shear layer near the separation point, leading to the generation of a row of vortices, and the generation of an unsteady irrotational field when these perturbations impinge the downstream corner. The upstream influence of this irrotational field provides further excitation of the unstable shear layer, closing the loop. Fig. 10(a) depicts the overall phase differences between the two corners of the cavity for the u_2 fluctuations and for the pressure disturbances at the fundamental frequency f_0 . The phase lag is equal to $1.5 \times 2\pi$ in both cases, indicating a vorticity–pressure coupling with always $N = 1.5$ aerodynamic cycles in the shear layer. The global criterion for these oscillations to be self-sustained is provided by the relation $N/f_0 = L/U_c + L/c_\infty$, where L/U_c is the time

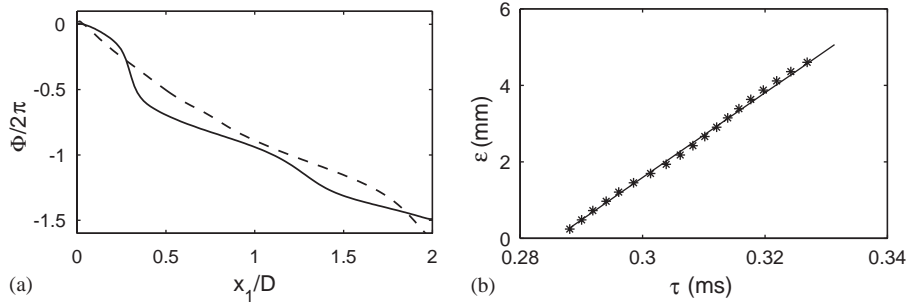


Fig. 10. Overall phase differences between the upstream and the downstream corners of the cavity (a) for the fundamental components of the pressure (—) and of the vertical velocity (---) fluctuations. Separation distance ϵ between the maxima of the correlation coefficients of the vertical velocity versus the time lag τ along the line $x_2 = 0$ (b). Correlation coefficients are evaluated every $\Delta x_1 = L/20$, with $x_1 = 0$ and $x_2 = 0$ as reference point. The slope gives the convection speed of the perturbations in the shear layer.

needed by the aerodynamic perturbations, convected at the speed U_c , to travel from the upstream to the downstream edge, and L/c_∞ is the time required for the pressure disturbances to propagate from the downstream to the upstream edge. The Strouhal number based on L is then given by

$$St_L = fL/U_\infty = N/(M + U_\infty/U_c). \quad (1)$$

The value of the convection velocity in the present case is given by the temporal evolution of the maxima of the cross-correlation coefficients along the line $x_2 = 0$. This evolution is seen to be linear in Fig. 10(b), and the slope provides the value $U_c = 0.65U_\infty$. Other simulations have shown that the value of the ratio U_c/U_∞ depends strongly on the simulation parameters, like the length L of the cavity. Formula (1), with $N = 1.5$ and $M = 0.7$, yields $St_L = 0.66$, in fairly good agreement with the value obtained by spectral analysis. This simple global model is similar to the Rossiter formula [32]. Nevertheless, the time lag α , introduced by Rossiter to corroborate measurements, is not required here. Moreover, N is not necessarily an integer but can take the form $n \pm 1/2$, with n an integer. Such half integer values have been observed in the studies by Sarohia [27] or Hussain and Zaman [33].

3. Application of integral methods

3.1. Introduction

In the present simulation, the acoustic part of the mesh represents more than the half of the total number of grid points, corresponding only to a propagation distance of six cavity depths. In order to ensure the six points per wavelength required by the numerical stencil for the smallest acoustic wavelength present in the computational domain (due to the strong steepening of wave fronts), the acoustic cut-off Strouhal number is $St_c = f_{max}L/U_\infty = L/(6\Delta y_{acous}M) \simeq 21$. Thus a reasonable calculation can include only few wavelengths whereas realistic problems require

observers at a distance of about two or three orders of magnitude greater than the cavity length. A direct acoustic calculation by DNS is difficult for such distances, especially for 3-D configurations.

The integral methods, instead, allow one to obtain the acoustic pressure at any point of the field, with a computational time independent of the observer distance. Typical calculations are carried out in two steps: an aerodynamic code based on CFD/CAA algorithms is used to evaluate the flow field, and then an integral formulation is applied to propagate the pressure disturbances to the far field. Integral methods rest upon two principal physical backgrounds. First, the acoustic analogies which split the computational domain into an aerodynamic region, where source terms responsible for the noise generation are built up, and an acoustic region governed by a linear wave equation. Second, the wave extrapolation methods which allow the evaluation of the far field once some quantities are known on a control surface. From a physical point of view, it is important to notice that the wave extrapolation methods are valid for any phenomena governed by the linear wave equation like optics, acoustics or electromagnetism while the acoustic analogy is based on the conservation laws of mass, momentum, and energy and is thus dedicated to aeroacoustics.

Recent advances in integral methods have been essentially developed for the reduction of helicopter rotor noise [34] and have been recently applied for predicting jet noise [35,36]. Zhang et al. [37] have used Curle's spatial formulation to obtain far-field spectra of cavity noise but no comparison was proposed.

3.2. Acoustic analogy

3.2.1. Formulation

The acoustic analogy was introduced by Lighthill [4] and was extended by Curle [38] and Ffowcs Williams and Hawkings [5] to include the effects of solid surfaces in arbitrary motion. The FW–H equation is an exact rearrangement of the continuity equation and Navier–Stokes equations into the form of an inhomogeneous wave equation with two surface source terms and a volume source term. The use of generalized functions to describe flow quantities allows one to embed the exterior flow problem in unbounded space. An integral solution can thus be obtained by convoluting the wave equation with the free-space Green function.

The original Lighthill analogy is written for an observation region at rest. For the case of a uniform flow, Ffowcs Williams and Hawkings proposed the use of a Lagrangian co-ordinate transform assuming the surface is moving in a fluid at rest. Following Goldstein [39], an inhomogeneous convected wave equation is considered in this study, including the convection effects in the wave operator.

For bidimensional geometries, it is more convenient to resolve this equation in the spectral domain [40,41]. A frequency-domain formulation avoids the evaluation of the retarded time, which can be a critical numerical point. The gain over the time domain applications is enhanced in 2-D because of the presence of the Heaviside function in the 2-D Green function. Whereas the classical Dirac in 3-D leads to a retarded time expression removing the temporal integration, the Heaviside function can only change the upper limit of the integration to a finite value, the lower limit remaining infinite. The spectral formulation removes this constraint. All the details of the derivation are provided in Appendix A.1, and the integral solution of the convected

FW–H equation is:

$$H(f)p'(\mathbf{x}, \omega) = - \int \int_{f>0} T_{ij}(\mathbf{y}, \omega) \frac{\partial^2 G(\mathbf{x}|\mathbf{y}, \omega)}{\partial y_i \partial y_j} d\mathbf{y} + \int_{f=0} F_i(\mathbf{y}, \omega) \frac{\partial G(\mathbf{x}|\mathbf{y}, \omega)}{\partial y_i} d\Sigma(\mathbf{y}), \quad (2)$$

where H is the Heaviside function, and the equation $f(\mathbf{y}) = 0$ defines the surface Σ outside of which the pressure field is calculated. The general expression of the source terms, given in Eqs. (A.10)–(A.12), have been simplified using the impermeability condition $u_n = \mathbf{u} \cdot \mathbf{n} = 0$ for rigid walls to give

$$T_{ij} = \rho(u_i - U_i^\infty)(u_j - U_j^\infty) + (p - c_\infty^2 \rho)\delta_{ij} - \tau_{ij}, \quad (3)$$

$$F_i = -[p\delta_{ij} - \tau_{ij}]n_j, \quad (4)$$

and the contribution of Q is zero in this case. In 2-D, the volume integral is restricted to a surface $S(f > 0)$ including the aerodynamic sources T_{ij} and the surface integral is calculated on the solid lines which represent rigid boundaries. The spatial derivatives are applied on the Green function, by using analytical formulae (A.13) and (A.14) to avoid the numerical differentiation of aerodynamic quantities, which could lead to numerical errors.

3.2.2. Numerical implementation

The first step is the storage of the aerodynamic quantities during one period of the DNS computation, using the pseudoperiodic behaviour of the oscillations in the cavity. The acoustic time step is 40 times the DNS time step which corresponds to 131 points per period. The variables (u_1, u_2, p, ρ) are recorded on the walls of the cavity (broken line of Fig. 11), and in the surface around it, depicted in Fig. 11: S_2 is the surface inside the cavity, and S_1 the surface above it. S_1 is $1D$ high, and extends from $-2D$ to $5D$ in the streamwise direction.

Second, the source terms T_{ij} and F_i are calculated and transformed into the frequency domain using the Fourier transform defined by (A.6). The integrals are then evaluated for each point of an acoustic meshgrid. This regular Cartesian grid of 176×184 points covers a area of $(-5D; 5D) \times (-1D; 8D)$. Lastly, an inverse Fourier transform is used to recover the acoustic signal in the time domain.

3.2.3. Results of the FW–H analogy

To obtain the contribution of surface sources (3) in the radiated sound field, the integrals over S_1 and S_2 are added (Fig. 12(a)). The line sources (4) are calculated on cavity walls with $M = 0.7$ (Fig. 12(b)).

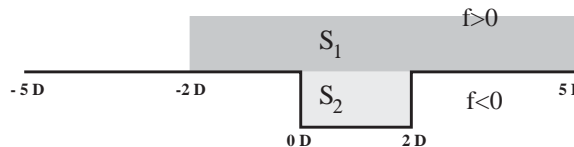


Fig. 11. Schematic of the physical broken line and surfaces for evaluation of FW–H analogy.

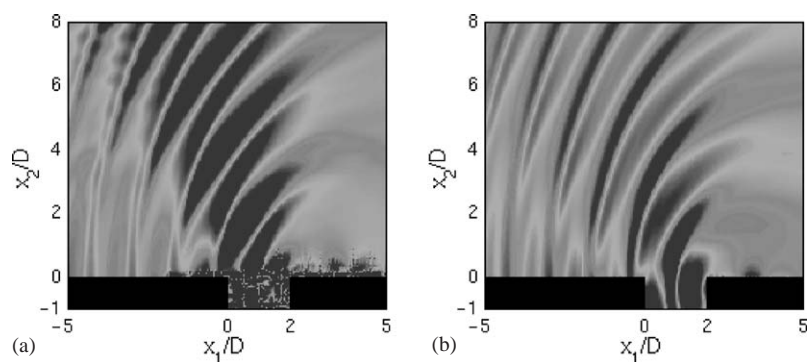


Fig. 12. Pressure field obtained corresponding to: (a) surface integral of the FW–H analogy, and (b) line integral of the FW–H analogy. The levels of the grayscale are between -3000 and 3000 Pa in both figures.

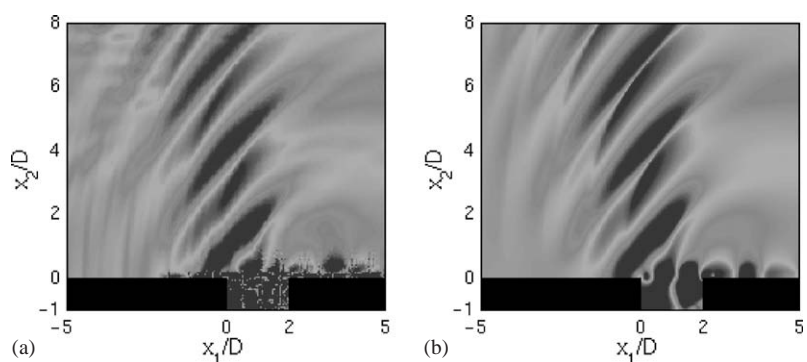


Fig. 13. Pressure field calculated at the same time by (a) FW–H analogy (line + surface integrals); (b) DNS reference solution. The grayscale levels are the same as in Fig. 12.

By summing the surface and line contributions (Fig. 13(a)), the total sound field is reconstructed in reasonably good agreement with the DNS reference solution of Fig. 13(b). Fig. 14 shows that the pressure profile along the line $x_1 + x_2 = 2D$ is consistent with the direct calculation of sound. However, small errors are visible, especially for long propagation distances. These discrepancies are due to truncation effects during the evaluation of surface integrals of T_{ij} . The principal truncation occurs in the streamwise direction where the source terms decrease slowly, leading to an extensive source abruptly cut by the end of the storage domain. This extensive region is due to the presence of advected vortices, ejected from the cavity during the clipping process, and feeding the reattached boundary layer on the downstream wall.

An analysis of the structure of the radiated field can be developed from the FW–H analogy results. Indeed, following the reflection theorem of Powell [42], it can be argued that volume integrals represent the direct radiated field, and surface integrals are essentially attributed to the reflected field due to cavity walls. These two fields at the same frequency give an interference figure where the two wave patterns are still distinguishable in the present case because the cavity is not compact at the oscillation frequency ($L/\lambda_0 = 0.47$).

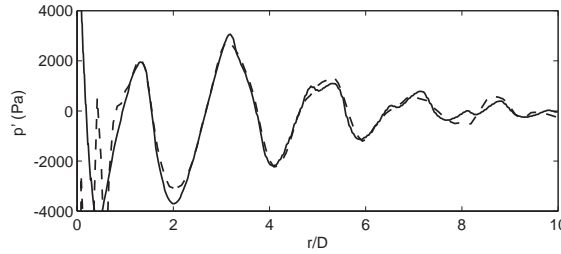


Fig. 14. Pressure profile along the line $x_1 + x_2 = 2D$ obtained by: FW–H analogy (---); DNS (—). $r = \sqrt{x_1^2 + x_2^2}$.

3.3. Wave extrapolation methods

This class of methods allows one to solve a linear wave propagation problem once some flow quantities are given on a closed fictitious surface surrounding all the sources. The most famous one is the Kirchhoff method which makes a parallel with electromagnetism by using Kirchhoff’s theorem [43]. The main advantage with respect to acoustic analogy approaches is that only surface integrals have to be evaluated because all non-linear quadrupole sources are assumed to be enclosed within the control surface. The problem is thus reduced by one dimension, which is particularly interesting from a numerical point of view. However, this approach suffers from the restriction that Kirchhoff’s surface must strictly be in the linear acoustic region. Brentner and Farassat [44] and Singer et al. [45] show some misleading results when Kirchhoff’s formulation is applied respectively to a hovering rotor blade and to the flow past a circular cylinder by using a control surface too close to the volume sources. The use of the FW–H equation for a permeable surface provides an alternative extrapolation method as noted in the original Ffowcs Williams and Hawkings’ paper [5]. This method has been recently implemented by di Francescantonio [46]. At nearly the same time, Brentner and Farassat [44] demonstrated the relationship between the FW–H equation and the Kirchhoff equation for moving surfaces. The FW–H and Kirchhoff formulations solve the same physical problem, the differences between the two methods being due to some choices made in the derivation process. This FW–H wave extrapolation method combines theoretically the flexibility of the Kirchhoff method and the physical insights of the FW–H equation.

3.3.1. The convected FW–H WEM

FW–H WEM denotes the WEM based on the FW–H formulation (A.9) by neglecting the volume integration (quadrupole source term T_{ij}). The analytical developments are the same as those of the FW–H analogy but the non-penetration condition $u_n = 0$ is no longer required, and, in order to obtain correct results, one has to allow a fluid flow across Σ . For a 2-D problem with uniform subsonic motion, FW–H WEM is given by Eq. (A.9) without the volume integral as

$$H(f)p'(\mathbf{x}, \omega) = \int_{f=0} F_i(\mathbf{y}, \omega) \frac{\partial G(\mathbf{x}|\mathbf{y}, \omega)}{\partial y_i} d\Sigma(\mathbf{y}) - \int_{f=0} i\omega Q(\mathbf{y}, \omega) G(\mathbf{x}|\mathbf{y}, \omega) d\Sigma(\mathbf{y}), \quad (5)$$

where the two source terms are

$$F_i = -[\rho(u_i - 2U_i^\infty)u_j + p\delta_{ij} - \tau_{ij}]n_j, \quad Q = \rho u_i n_i. \quad (6, 7)$$

This method is sometimes called porous FW–H because it coincides with the application of FW–H analogy on a fictitious porous surface enclosing all sound sources.

3.3.2. The convected Kirchhoff method

The 2-D frequency domain form of the Kirchhoff formulation, including the effect of a mean flow in the observation region is derived in Appendix A.2 and can be written as

$$\begin{aligned} H(f)p'(\mathbf{x}, \omega) = & \frac{i\beta}{4} \int_{f=0} \left\{ \frac{\partial p(\mathbf{y}, \omega)}{\partial n_\beta} H_0^{(2)}\left(\frac{k}{\beta^2} r_\beta\right) + \frac{k}{\beta^2} p(\mathbf{y}, \omega) \left[\frac{\partial r_\beta}{\partial n_\beta} H_1^{(2)}\left(\frac{k}{\beta^2} r_\beta\right) \right. \right. \\ & \left. \left. - iM \frac{\partial y_1}{\partial n_\beta} H_0^{(2)}\left(\frac{k}{\beta^2} r_\beta\right) \right] \times \exp\left(i \frac{Mk(x_1 - y_1)}{\beta^2}\right) \right\} d\Sigma_\beta. \end{aligned} \quad (8)$$

3.3.3. Numerical implementation

From an algorithmic point of view, there is almost no difference between the different integral formulations considered here, and the numerical implementation follows the same steps as for the FW–H analogy. The recording time step is also 40 times the DNS time step. In the convected Kirchhoff method, the pressure distribution and its normal derivative over the three lines L_1 , L_2 , and L_3 spanning the longitudinal direction are needed to perform the integration. The first line L_1 is chosen in the acoustic region at $y_2 = 1D$, the second line L_2 is in the near-field region at $y_2 = 0.5D$, and the third line L_3 is still closer to the shear at $y_2 = 0.2D$. The normal derivative $\partial p/\partial y_2$ is not directly available from the near-field solution and is here calculated with the DRP scheme. The variables (u_1, u_2, p, ρ) are recorded on the same three fictitious lines for the FW–H WEM (Fig. 15). The integrals are then evaluated on the 176×184 meshgrid, already used for the application of the FW–H analogy.

3.3.4. Results of porous FW–H

The results of integration over L_1 , L_2 , and L_3 with source terms defined by Eqs. (6) and (7), and with $M = 0.7$ in the observer domain are compared in Fig. 16. The three pressure fields obtained are consistent with the DNS. The contour plots are sharper when the line is farther from sources. This is confirmed by the pressure profile of Fig. 17. The three profiles predicted by the FW–H WEM are in good agreement with the DNS result. The small differences could be attributed to the fact that not all of the quadrupole sources are taken into account when the integration line is too close to the walls.

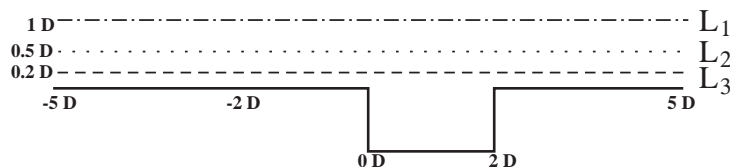


Fig. 15. Schematic of the different fictitious lines for evaluation of WEM.

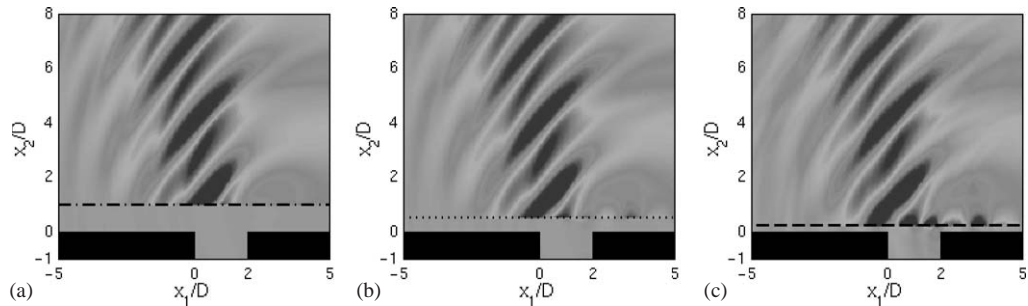


Fig. 16. Pressure field calculated at the same time by (a) FW–H WEM from L_1 , (b) FW–H WEM from L_2 , (c) FW–H WEM from L_3 . The grayscale levels are the same as in Fig. 12.

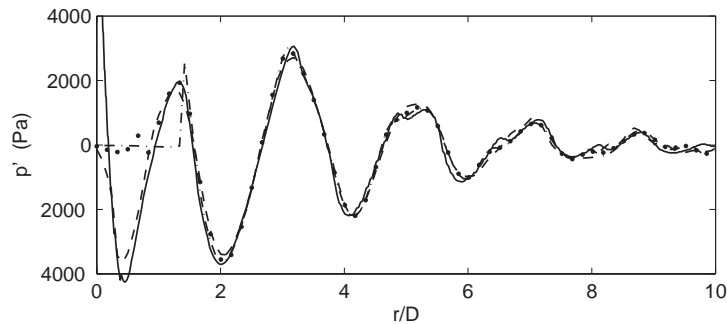


Fig. 17. Pressure profile along the line $x_1 + x_2 = 2D$ obtained by: $- \cdot -$, FW–H-WEM from L_1 ; \dots , FW–H-WEM from L_2 ; $- - -$, FW–H-WEM from L_3 ; $-$, DNS. $r = \sqrt{x_1^2 + x_2^2}$.

3.3.5. Results of convected Kirchhoff method

In the Kirchhoff method, the results of the integration of Eq. (8) over L_1 , L_2 , and L_3 are depicted in Fig. 18. The computed far-fields are consistent with that of DNS depicted in Fig. 13(b), even when the control line is located in the near-field region. The contour plots are only a little sharper when the line is farther from the sources because more non-linear effects are included in the control line. The pressure profiles along the line $x_1 + x_2 = 2D$ of Fig. 19 are also consistent with direct calculation. The amplitudes, evaluated from L_1 , L_2 , and L_3 , are zero for r respectively lower than $\sqrt{2}$, $\sqrt{2}/2$, and $\sqrt{2}/5$, since observation points then lie inside the control line ($H(f) = 0$).

3.3.6. Comparison of the integral methods

The results obtained with Kirchhoff's method are similar to those using the permeable form of the FW–H equation. In this configuration, the additional non-linear terms appearing in the surface integrals of FW–H WEM but missing in the Kirchhoff formulation, as noted by Brentner and Farassat [44], do not play a significant role and do not lead to the drastic differences observed in some previous comparisons when the control surface is too close to the sources [44,45]. Like di Francescantonio [46] or Prieur and Rahier [47], a similar behaviour of the two extrapolation

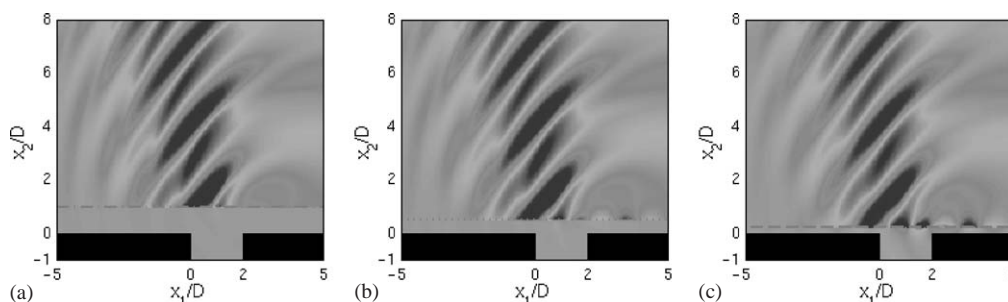


Fig. 18. Pressure field calculated at the same time by (a) Kirchhoff's method from L_1 ; (b) Kirchhoff's method from L_2 ; (c) Kirchhoff's method from L_3 . The grayscale levels are the same as in Fig. 12.

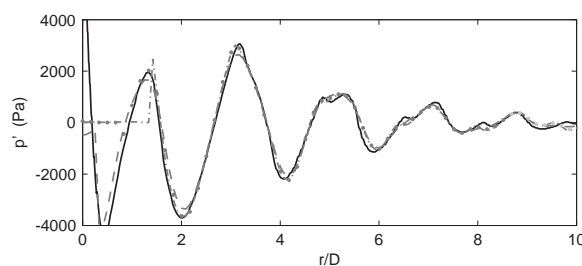


Fig. 19. Pressure profile along the line $x_1 + x_2 = 2D$ obtained by: $- \cdot - \cdot$ (in gray), Kirchhoff's WEM from L_1 , (\dots) (in gray), Kirchhoff's WEM from L_2 , $(- - -)$ (in gray), Kirchhoff's WEM from L_3 , $(—)$ (in gray), DNS. $r = \sqrt{x_1^2 + x_2^2}$.

methods is noticed. In the present application, the results are relatively insensitive to the location of the extrapolation line since the quadrupole sources are essentially below the lower extrapolation line. The advantage of the porous FW–H method is only the fact that it uses directly the quantities computed by the direct simulation without the need for further numerical processing.

Fig. 20 presents the temporal evolutions of the pressure over one period using the three methods. DNS results show a very stiff slope for the temporal evolution, which indicates a non-linear propagation. This is due to the high level pressure waves generated by the interaction with the downstream corner of the cavity. However, the three integral formulation time traces have a smoother shape. The non-linear propagation is indeed not described by the convected wave operator derived for the different integral methods. Only the non-linear effects inside the source surface for the FW–H analogy and below the control lines for the WEM are taken into account.

The temporal evolutions over a period provide the overall sound pressure directivity on a circle of radius $7D$ centred on the downstream corner of the cavity, in Fig. 21. The discrepancies for the two extrapolation methods are of the order of 1 dB. Larger errors are noted for the FW–H analogy, especially in the downstream direction, where the truncation effects are sensitive. The FW–H analogy is less accurate than the WEM but provides more information on wave structure. It is also more expensive in CPU time because of the evaluation of the volume integral (surface integral in 2-D) whereas wave extrapolation methods need only surface integral (line integral in 2-D).

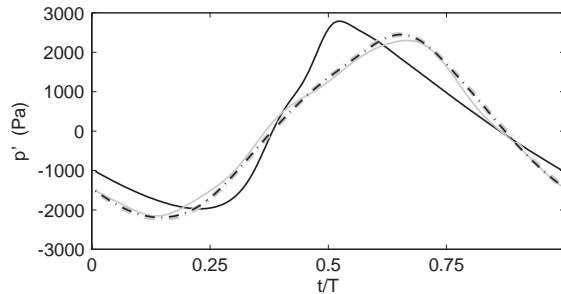


Fig. 20. Time traces of fluctuating pressure over an oscillation period $T = 1/f_0$ at the point $x_1/D = -1.28$ and $x_2/D = 6.14$. \cdots (in gray), Kirchhoff's method from L_1 ; $- \cdot - \cdot$, FW-H-WEM from L_1 ; $-$ (in gray), FW-H analogy; $-$, DNS.

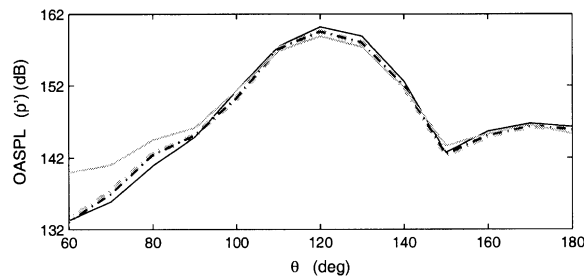


Fig. 21. Overall sound pressure level as function of θ measured from streamwise axis, with centre at the downstream edge of the cavity, evaluated on the sensors reported in Fig. 1. \cdots (in gray), Kirchhoff's method from L_1 ; $- \cdot - \cdot$ (in gray), FW-H-WEM from L_1 ; $-$ (in gray), FW-H analogy; $-$, DNS.

4. Conclusion

In the first part, a direct calculation of the sound radiated by a flow over a 2-D rectangular cavity is carried out. To this end, a DNS is performed using CAA numerical methods. This approach is expensive but is able to give all the interactions between flow and acoustics and provides a powerful tool to determine noise generation mechanisms. The directly computed sound field is consistent with corresponding results of Karamcheti's experiments.

The results of DNS are then successfully compared to three hybrid methods which use the DNS quantities to solve integral formulations. The wave extrapolation methods, like the Kirchhoff or the porous FW-H methods, are relatively unaffected by the location of the control surface and constitute interesting complementary tools to extend CAA near field to the far field. The acoustic analogy is less efficient because volume integrations are costly and sensitive to truncation effects. Nevertheless, it allows a separation between direct and reflected sound fields, which is useful for an analysis of radiation patterns.

To extend the present investigation, a 3-D simulation should be carried out. The recirculation zone inside the cavity is indeed characterized by a 3-D turbulent mixing, even if the development of the shear layer is almost 2-D. Such a study is reported in Ref. [48].

Acknowledgements

Computing time is supplied by Institut du Développement et des Ressources en Informatique Scientifique (IDRIS-CNRS). The authors would like to thank Christophe Bogey for providing ALESIA code for free flows, and for many useful discussions and suggestions during the course of this work.

Appendix A

A.1. Derivation of convected FW–H analogy

In order to derive the inhomogeneous, uniformly moving medium wave equation, the continuity and momentum equations are rewritten using the derivative for an observer moving along with the mean flow, defined as

$$\mathbf{D}_\infty / \mathbf{D}t = \partial / \partial t + U_i^\infty \partial / \partial x_i, \quad (\text{A.1})$$

where U_i^∞ are the components of the uniform mean velocity in the observer domain. The continuity equation becomes

$$\frac{\mathbf{D}_\infty}{\mathbf{D}t} \rho = -\frac{\partial \rho u_i}{\partial x_i} + U_i^\infty \frac{\partial \rho}{\partial x_i} = -\frac{\partial \rho(u_i - U_i^\infty)}{\partial x_i} = -\frac{\partial \rho \tilde{u}_i}{\partial x_i},$$

where $\tilde{u}_i = u_i - U_i^\infty$. To take into account the presence of a surface Σ , defined by the equation $f(\mathbf{y}) = 0$, the latter equation is multiplied by the Heaviside function $H(f)$, and $H(f)$ is introduced inside the differential operators,

$$\begin{aligned} \frac{\mathbf{D}_\infty}{\mathbf{D}t} [(\rho - \rho_\infty)H(f)] + \frac{\partial}{\partial x_i} [\rho \tilde{u}_i H(f)] &= (\rho - \rho_\infty) \frac{\mathbf{D}_\infty H(f)}{\mathbf{D}t} + \rho \tilde{u}_i \frac{\partial H(f)}{\partial x_i} \\ &= (\rho - \rho_\infty) U_i^\infty \frac{\partial H(f)}{\partial x_i} + \rho \tilde{u}_i \frac{\partial H(f)}{\partial x_i}, \end{aligned} \quad (\text{A.2})$$

by noting that Σ is a stationary surface. Similarly, for the momentum equation, this yields

$$\begin{aligned} \frac{\mathbf{D}_\infty}{\mathbf{D}t} (\rho \tilde{u}_i) &= \frac{\partial}{\partial t} [\rho(u_i - U_i^\infty)] + U_j^\infty \frac{\partial}{\partial x_j} [\rho(u_i - U_i^\infty)] \\ &= -\frac{\partial p}{\partial x_i} + \frac{\partial \tau_{ij}}{\partial x_j} - \frac{\partial \rho u_i u_j}{\partial x_j} + U_i^\infty \frac{\partial \rho u_j}{\partial x_j} + U_j^\infty \frac{\partial \rho u_i}{\partial x_j} - U_i^\infty U_j^\infty \frac{\partial \rho}{\partial x_j}. \end{aligned}$$

By making use of the equality

$$\frac{\partial}{\partial x_j} (\rho \tilde{u}_i \tilde{u}_j) = \frac{\partial \rho u_i u_j}{\partial x_j} - U_i^\infty \frac{\partial \rho u_j}{\partial x_j} - U_j^\infty \frac{\partial \rho u_i}{\partial x_j} + U_i^\infty U_j^\infty \frac{\partial \rho}{\partial x_j},$$

the momentum equation reduces to

$$\frac{\mathbf{D}_\infty}{\mathbf{D}t} (\rho \tilde{u}_i) = -\frac{\partial p}{\partial x_i} + \frac{\partial \tau_{ij}}{\partial x_j} - \frac{\partial \rho \tilde{u}_i \tilde{u}_j}{\partial x_j},$$

which can also be written as

$$\frac{D_\infty}{Dt} \rho \tilde{u}_i + c_\infty^2 \frac{\partial(\rho - \rho_\infty)}{\partial x_i} = -\frac{\partial T_{ij}}{\partial x_j},$$

where $T_{ij} = \rho \tilde{u}_i \tilde{u}_j + (p - c_\infty^2(\rho - \rho_\infty))\delta_{ij} - \tau_{ij}$.

With the introduction of generalized functions, this yields

$$\begin{aligned} \frac{D_\infty}{Dt} [\rho \tilde{u}_i H(f)] + c_\infty^2 \frac{\partial}{\partial x_i} [(\rho - \rho_\infty) H(f)] \\ = -\frac{\partial}{\partial x_j} [T_{ij} H(f)] + [\rho \tilde{u}_i \tilde{u}_j + p \delta_{ij} - \tau_{ij}] \frac{\partial H(f)}{\partial x_j} + \rho \tilde{u}_i U_j^\infty \frac{\partial H(f)}{\partial x_j}. \end{aligned} \quad (A.3)$$

Now the convected wave equation for $(\rho - \rho_\infty)H(f)$ is formed by applying the operator D_∞/Dt to Eq. (A.2). The divergence of Eq. (A.3) is taken, and the two equations are subtracted. This leads to

$$\begin{aligned} \left\{ \frac{D_\infty^2}{Dt^2} - c_\infty^2 \frac{\partial^2}{\partial x_i^2} \right\} [(\rho - \rho_\infty) H(f)] = \frac{\partial^2}{\partial x_i \partial x_j} [T_{ij} H(f)] + \frac{D_\infty}{Dt} \left[((\rho - \rho_\infty) U_i^\infty + \rho \tilde{u}_i) \delta(f) \frac{\partial f}{\partial x_i} \right] \\ - \frac{\partial}{\partial x_i} \left[(p \delta_{ij} - \tau_{ij} + \rho \tilde{u}_i \tilde{u}_j + \rho \tilde{u}_i U_j^\infty) \delta(f) \frac{\partial f}{\partial x_j} \right]. \end{aligned}$$

The material derivative in the right side is then developed to give

$$\begin{aligned} \left\{ \frac{D_\infty^2}{Dt^2} - c_\infty^2 \frac{\partial^2}{\partial x_i^2} \right\} [(\rho - \rho_\infty) H(f)] = \frac{\partial^2}{\partial x_i \partial x_j} [T_{ij} H(f)] + \frac{\partial}{\partial t} \left[((\rho - \rho_\infty) U_i^\infty + \rho \tilde{u}_i) \delta(f) \frac{\partial f}{\partial x_i} \right] \\ + \frac{\partial}{\partial x_i} \left[((\rho - \rho_\infty) U_i^\infty U_j^\infty + \rho \tilde{u}_j U_i^\infty) \delta(f) \frac{\partial f}{\partial x_j} \right] \\ - \frac{\partial}{\partial x_i} \left[(p \delta_{ij} - \tau_{ij} + \rho \tilde{u}_i \tilde{u}_j + \rho \tilde{u}_i U_j^\infty) \delta(f) \frac{\partial f}{\partial x_j} \right]. \end{aligned}$$

Lastly, the terms are regrouped in the form

$$\begin{aligned} \left\{ \frac{D_\infty^2}{Dt^2} - c_\infty^2 \frac{\partial^2}{\partial x_i^2} \right\} [(\rho - \rho_\infty) H(f)] = \left\{ \frac{\partial^2}{\partial t^2} + U_i^\infty U_j^\infty \frac{\partial^2}{\partial x_i \partial x_j} + 2U_i^\infty \frac{\partial^2}{\partial x_i t} - c_\infty^2 \frac{\partial^2}{\partial x_i^2} \right\} [\rho' H(f)] \\ = \frac{\partial^2}{\partial x_i \partial x_j} [T_{ij} H(f)] + \frac{\partial}{\partial x_i} [F_i \delta(f)] + \frac{\partial}{\partial t} [Q \delta(f)], \end{aligned} \quad (A.4)$$

where

$$\begin{aligned} T_{ij} &= \rho(u_i - U_i^\infty)(u_j - U_j^\infty) + (p - c_\infty^2(\rho - \rho_\infty))\delta_{ij} - \tau_{ij}, \\ F_i &= -[\rho(u_i - 2U_i^\infty)u_j + \rho_\infty U_i^\infty U_j^\infty + p\delta_{ij} - \tau_{ij}] \frac{\partial f}{\partial x_j}, \\ Q &= [\rho u_i - \rho_\infty U_i^\infty] \partial f / \partial x_i. \end{aligned} \quad (A.5)$$

With application of the Fourier transform

$$F[\phi(\mathbf{x}, t)] = \phi(\mathbf{x}, \omega) = \int_{-\infty}^{\infty} \phi(\mathbf{x}, t) e^{-i\omega t} dt, \quad (A.6)$$

and suppressing the time factor $\exp(i\omega t)$, Eq. (A.4) becomes

$$\begin{aligned} & \left\{ \frac{\partial^2}{\partial x_i^2} + k^2 - 2iM_i k \frac{\partial}{\partial x_i} - M_i M_j \frac{\partial^2}{\partial x_i \partial x_j} \right\} [H(f)c_\infty^2 \rho'(\mathbf{x}, \omega)] \\ & = -\frac{\partial^2}{\partial x_i \partial x_j} [T_{ij}(\mathbf{x}, \omega)H(f)] - \frac{\partial}{\partial x_i} [F_i(\mathbf{x}, \omega)\delta(f)] - i\omega Q(\mathbf{x}, \omega)\delta(f), \end{aligned} \quad (\text{A.7})$$

where $M_i = U_i^\infty / c_\infty$. The Green function G of this convected Helmholtz equation is obtained from a Prandtl–Glauert transformation of the 2-D free-space Green function in the frequency domain, which leads to

$$G(\mathbf{x}|\mathbf{y}, \omega) = \frac{i}{4\beta} e^{i(Mk(x_1 - y_1)/\beta^2)} H_0^{(2)}\left(\frac{k}{\beta^2} r_\beta\right), \quad (\text{A.8})$$

where $r_\beta = \sqrt{(x_1 - y_1)^2 + \beta^2(x_2 - y_2)^2}$, $H_0^{(2)}$ is the Hankel function of the second kind and order zero, $\beta = \sqrt{1 - M^2}$ is the Prandtl–Glauert factor, $M < 1$, \mathbf{x} is the observer position, and \mathbf{y} denotes a source point. By convoluting Eq. (A.7) with the Green function (A.8), and by using the properties of the convolution product, denoted by $*$, the solution can be expressed as

$$\begin{aligned} [p'H(f)](\mathbf{x}, \omega) & = -\frac{\partial^2 [T_{ij}H(f)]}{\partial x_i \partial x_j} * G - \frac{\partial [F_i \delta(f)]}{\partial x_i} * G - i\omega [Q\delta(f)] * G \\ & = -\frac{\partial^2}{\partial x_i \partial x_j} [T_{ij}H(f) * G] - \frac{\partial}{\partial x_i} [F_i \delta(f) * G] - i\omega [Q\delta(f) * G] \\ & = -[T_{ij}H(f)] * \frac{\partial^2 G}{\partial x_i \partial x_j} - [F_i \delta(f)] * \frac{\partial G}{\partial x_i} - i\omega [Q\delta(f)] * G. \end{aligned}$$

By noting that $\partial G / \partial x_i = -\partial G / \partial y_i$, the integral solution of Eq. (A.7) is given by

$$\begin{aligned} H(f)p'(\mathbf{x}, \omega) & = \int_{f=0} F_i(\mathbf{y}, \omega) \frac{\partial G(\mathbf{x}|\mathbf{y}, \omega)}{\partial y_i} d\Sigma - \int_{f=0} i\omega Q(\mathbf{y}, \omega) G(\mathbf{x}|\mathbf{y}, \omega) d\Sigma \\ & \quad - \int \int_{f>0} T_{ij}(\mathbf{y}, \omega) \frac{\partial^2 G(\mathbf{x}|\mathbf{y}, \omega)}{\partial y_i \partial y_j} dy, \end{aligned} \quad (\text{A.9})$$

where the source terms (A.5) can be written as

$$T_{ij} = \rho(u_i - U_i^\infty)(u_j - U_j^\infty) + (p - c_\infty^2 \rho)\delta_{ij} - \tau_{ij}, \quad (\text{A.10})$$

$$F_i = -[\rho(u_i - 2U_i^\infty)u_j + p\delta_{ij} - \tau_{ij}]n_j, \quad Q = \rho u_i n_i. \quad (\text{A.11, A.12})$$

The function $f = 0$ is scaled so that $\partial f / \partial x_j = n_j$, the j -component of the unit normal vector pointing toward the observer domain ($f > 0$). The expressions have also been simplified by removing the constant terms, $c_\infty^2 \rho_\infty \delta_{ij}$ in T_{ij} , $\rho_\infty U_i^\infty U_j^\infty n_j$ in F_i , and $\rho_\infty U_i^\infty n_i$ in Q , which do not radiate sound.

In expression (A.9), the derivatives of the Green function are evaluated analytically, which gives for the first derivatives

$$\begin{aligned}\frac{\partial G(\mathbf{x}|\mathbf{y}, \omega)}{\partial y_1} &= -A(r_1) \left\{ \frac{iMk}{\beta^2} H_0^{(2)}\left(\frac{kr_\beta}{\beta^2}\right) - \frac{k}{\beta^2} \frac{r_1}{r_\beta} H_1^{(2)}\left(\frac{kr_\beta}{\beta^2}\right) \right\}, \\ \frac{\partial G(\mathbf{x}|\mathbf{y}, \omega)}{\partial y_2} &= A(r_1) \left\{ \frac{kr_2}{r_\beta} H_1^{(2)}\left(\frac{kr_\beta}{\beta^2}\right) \right\},\end{aligned}\quad (\text{A.13})$$

and for the second derivatives

$$\begin{aligned}\frac{\partial^2 G(\mathbf{x}|\mathbf{y}, \omega)}{\partial y_1 \partial y_2} &= -A(r_1) \left\{ \frac{k^2}{\beta^2} \frac{r_1 r_2}{r_\beta^2} H_0^{(2)}\left(\frac{kr_\beta}{\beta^2}\right) + \frac{kr_2}{r_\beta} \left(\frac{iMk}{\beta^2} - \frac{2r_1}{r_\beta^2} \right) H_1^{(2)}\left(\frac{kr_\beta}{\beta^2}\right) \right\} \\ \frac{\partial^2 G(\mathbf{x}|\mathbf{y}, \omega)}{\partial y_1^2} &= -A(r_1) \frac{k^2}{\beta^4} \left\{ \left(M^2 + \frac{r_1^2}{r_\beta^2} \right) H_0^{(2)}\left(\frac{kr_\beta}{\beta^2}\right) \right. \\ &\quad \left. + \left(\frac{2iMr_1}{r_\beta} - \frac{\beta^2 r_1^2 - \beta^2 r_2^2}{k r_\beta^3} \right) H_1^{(2)}\left(\frac{kr_\beta}{\beta^2}\right) \right\}\end{aligned}\quad (\text{A.14})$$

$$\frac{\partial^2 G(\mathbf{x}|\mathbf{y}, \omega)}{\partial y_2^2} = -A(r_1) \left\{ \frac{k^2 r_2^2}{r_\beta^2} H_0^{(2)}\left(\frac{kr_\beta}{\beta^2}\right) + \frac{k}{r_\beta} \left(\frac{r_1^2 - \beta^2 r_2^2}{r_\beta^2} \right) H_1^{(2)}\left(\frac{kr_\beta}{\beta^2}\right) \right\},$$

where $r_i = x_i - y_i$, and $A(r_1) = \frac{i}{4\beta} \exp\left(\frac{iMkr_1}{\beta^2}\right)$.

A.2. Derivation of convected Kirchhoff method

For a moving medium, the acoustic pressure at an arbitrary point \mathbf{x} and time t is related to the distribution Q of sources within V and the distribution of the pressure and its derivative on the boundary of V , $\Sigma(f=0)$, by the generalized Green formula [39]. For a 2-D configuration, with $\mathbf{U}_\infty = (U_\infty, 0)$ in the observer domain, it can be written as

$$\begin{aligned}H(f)p'(\mathbf{x}, t) &= \int_{-\infty}^{\infty} \int \int_{V(f>0)} Q(\mathbf{y}, \tau) G(\mathbf{x}, t|\mathbf{y}, \tau) \, d\mathbf{y} \, d\tau \\ &\quad + \int_{-\infty}^{\infty} \int_{\Sigma} \left\{ G \frac{\partial p}{\partial y_i} - p \frac{\partial G}{\partial y_i} \right\} n_i \, d\Sigma \, d\tau \\ &\quad + \frac{U_\infty}{c_\infty^2} \int_{-\infty}^{\infty} \int_{\Sigma} \left\{ p \frac{D G}{D \tau} - G \frac{D p}{D \tau} \right\} n_i \, d\Sigma \, d\tau,\end{aligned}\quad (\text{A.15})$$

where $D/Dt = \partial/\partial t + U_\infty \partial/\partial x_1$ is the time rate of change seen by an observer moving along with the mean flow, and G is the Green function solution to the uniformly moving medium wave equation. By taking the Fourier transform (A.6), with the time factor $\exp(i\omega t)$ suppressed,

formula (A.15) reduces to the form

$$\begin{aligned} H(f)p'(\mathbf{x}, \omega) &= \int \int_{V(\mathbf{y})} Q(\mathbf{y}, \omega) G(\mathbf{x}|\mathbf{y}, \omega) d\mathbf{y} \\ &+ \int_{\Sigma} \left\{ G(\mathbf{x}|\mathbf{y}, \omega) \frac{\partial p(\mathbf{y}, \omega)}{\partial y_i} - p(\mathbf{y}, \omega) \frac{\partial G(\mathbf{x}|\mathbf{y}, \omega)}{\partial y_i} \right\} (n_i - M^2 n_i) d\Sigma(\mathbf{y}) \\ &- 2i\omega \frac{M}{c_{\infty}} \int_{\Sigma} p(\mathbf{y}, \omega) G(\mathbf{x}|\mathbf{y}, \omega) n_i d\Sigma(\mathbf{y}), \end{aligned} \quad (\text{A.16})$$

where $M = U_{\infty}/c_{\infty}$. The first derivative of the convected Green function in the frequency domain (A.8) is expressed as

$$\frac{\partial G(\mathbf{x}|\mathbf{y}, \omega)}{\partial y_i} = \frac{i}{4\beta} \exp\left(i \frac{Mkr_1}{\beta^2}\right) \left\{ -\frac{k}{\beta^2} \frac{\partial r_{\beta}}{\partial y_i} H_1^{(2)}\left(\frac{k}{\beta^2} r_{\beta}\right) - i \frac{Mk}{\beta^2} \frac{\partial y_1}{\partial y_i} H_0^{(2)}\left(\frac{k}{\beta^2} r_{\beta}\right) \right\},$$

and, by assuming that all the volume sources Q are included in Σ , (A.16) becomes

$$\begin{aligned} H(f)p'(\mathbf{x}, \omega) &= \frac{i}{4\beta} \int_{\Sigma} \left\{ \frac{\partial p(\mathbf{y}, \omega)}{\partial y_i} H_0^{(2)}\left(\frac{k}{\beta^2} r_{\beta}\right) + \frac{kp(\mathbf{y}, \omega)}{\beta^2} \left[\frac{\partial r_{\beta}}{\partial y_i} H_1^{(2)}\left(\frac{k}{\beta^2} r_{\beta}\right) \right. \right. \\ &\left. \left. + iM \frac{\partial y_1}{\partial y_i} H_0^{(2)}\left(\frac{k}{\beta^2} r_{\beta}\right) - 2iM \frac{\partial y_1}{\partial y_i} H_0^{(2)}\left(\frac{k}{\beta^2} r_{\beta}\right) \right] \right\} \times \exp\left(i \frac{Mkr_1}{\beta^2}\right) (n_i - M^2 n_i) d\Sigma. \end{aligned} \quad (\text{A.17})$$

By applying the Prandtl–Glauert transform to \mathbf{n} and $d\Sigma$, respectively, denoted \mathbf{n}_{β} and $d\Sigma_{\beta}$, expression (8) is obtained.

References

- [1] D. Rockwell, Oscillations of impinging shear layers, *AIAA Journal* 21 (5) (1983) 645–664.
- [2] D. Rockwell, E. Naudascher, Review—self-sustaining oscillations of flow past cavities, *ASME Journal of Fluids Engineering* 100 (1978) 152–165.
- [3] C. Bogey, C. Bailly, D. Juvé, Noise investigation of a high subsonic, moderate Reynolds number jet using a compressible LES, *Theoretical and Computational Fluid Dynamics* 16 (4) (2003) 273–297.
- [4] M.J. Lighthill, On sound generated aerodynamically I. General theory, *Proceedings of the Royal Society of London A* 211 (1952) 564–587.
- [5] J.E. Ffowcs Williams, D.L. Hawkings, Sound generated by turbulence and surfaces in arbitrary motion, *Philosophical Transactions of the Royal Society, A* 264 (1151) (1969) 321–342.
- [6] F. Farassat, M.K. Myers, Extension of Kirchhoff's formula to radiation from moving surfaces, *Journal of Sound and Vibration* 123 (3) (1988) 451–460.
- [7] K. Karamcheti, Acoustic radiation from two-dimensional rectangular cutouts in aerodynamic surfaces, *Technical Note 3487, NACA*, 1955, pp. 1–33.
- [8] W.L. Hankey, J.S. Shang, Analyses of pressure oscillations in an open cavity, *AIAA Journal* 18 (8) (1980) 892–898.
- [9] S.A. Slimon, D.W. Davis, C.A. Wagner, Far-field aeroacoustic computation of unsteady cavity flow, 36th Aerospace Science Meeting & Exhibition, *AIAA 98-0285*, 1998.
- [10] C.-J. Tam, P.D. Orkwis, P.J. Disimile, Comparison of Baldwin–Lomax turbulence models for two-dimensional open cavity computations, *AIAA Journal* 34 (3) (1995) 629–631.
- [11] A. Rona, W. Dieudonné, A flow-resonant model of transonic laminar open cavity instability, *AIAA Paper 2000-1967*, 2000.
- [12] X. Zhang, Compressible cavity flow oscillation due to shear layer instabilities and pressure feedback, *AIAA Journal* 33 (8) (1995) 1404–1411.

- [13] T. Colonius, A.J. Basu, C.W. Rowley, Numerical investigation of the flow past a cavity, AIAA Paper 99-1912, 1999.
- [14] C.M. Shieh, P.J. Morris, Parallel numerical simulation of subsonic cavity noise, AIAA Paper 99-1891, 1999.
- [15] M. Gharib, A. Roshko, The effect of flow oscillations on cavity drag, *Journal of Fluid Mechanics* 177 (1981) 501–530.
- [16] X. Gloerfelt, C. Bailly, D. Juvé, Calcul direct du rayonnement acoustique d'un écoulement affleurant une cavité, *Comptes Rendus de l'Académie des Sciences (Série IIB)* 328 (2000) 625–631.
- [17] C.M. Shieh, P.J. Morris, Parallel computational aeroacoustic simulation of turbulent subsonic cavity flow, AIAA Paper 2000-1914, 2000.
- [18] H.N. Najm, A.F. Ghoniem, Numerical simulation of the convective instability in a dump combustor, *AIAA Journal* 29 (6) (1991) 911–919.
- [19] C. Bogey, Calcul Direct du Bruit Aérodynamique et Validation de Modèles Acoustiques Hybrides, Ph.D. Thesis, Ecole Centrale de Lyon, No 2000-11, Ecully, 2000.
- [20] C.K.W. Tam, J.C. Webb, Dispersion-relation-preserving finite difference schemes for computational acoustics, *Journal of Computational Physics* 107 (1993) 262–281.
- [21] C.K.W. Tam, Z. Dong, Radiation and outflow boundary conditions for direct computation of acoustic and flow disturbances in a nonuniform mean flow, *Journal of Computational Acoustics* 4 (2) (1996) 175–201.
- [22] C. Bogey, C. Bailly, D. Juvé, Numerical simulation of sound generated by vortex pairing in a mixing layer, *AIAA Journal* 38 (12) (2000) 2210–2218.
- [23] S.N. Sinha, A.K. Gupta, M.M. Oberai, Laminar separating flow over backsteps and cavities, Part ii: cavities, *AIAA Journal* 20 (3) (1982) 370–375.
- [24] N. Forestier, Etude Expérimentale d'une Couche Cisailée au-dessus d'une Cavité en Régime Transonique, Ph.D. Thesis, Ecole Centrale de Lyon, No NT 2001-1, Ecully, 2001.
- [25] C.-M. Ho, L.-S. Huang, Subharmonics and vortex merging in mixing layers, *Journal of Fluid Mechanics* 119 (1982) 443–473.
- [26] D. Oster, I. Wygnanski, The forced mixing layer between parallel streams, *Journal of Fluid Mechanics* 123 (1982) 91–130.
- [27] V. Sarohia, Experimental oscillations in flows over shallow cavities, *AIAA Journal* 15 (7) (1977) 984–991.
- [28] J.C. Lin, D. Rockwell, Organized oscillations of initially turbulent flow past a cavity, *AIAA Journal* 39 (6) (2001) 1139–1151.
- [29] D. Rockwell, C. Knisely, The organized nature of flow impingement upon a corner, *Journal of Fluid Mechanics* 93 (1979) 413–432.
- [30] S. Ziada, D. Rockwell, Vortex-leading-edge interaction, *Journal of Fluid Mechanics* 118 (1982) 79–107.
- [31] A.C. Kistler, F.C. Tan, Some properties of turbulent separated flows, *The Physics of Fluids, Supplement, Boundary Layers and Turbulence* 10 (1967) S165–S173.
- [32] J.E. Rossiter, Wind-tunnel experiments on the flow over rectangular cavities at subsonic and transonic speeds, Technical Report 3438, Aeronautical Research Council Reports and Memoranda, 1964.
- [33] A.K.M.F. Hussain, K.B.M.Q. Zaman, The free shear layer tone phenomenon and probe interference, *Journal of Fluid Mechanics* 87 (2) (1978) 349–383.
- [34] K.S. Brentner, Modeling aerodynamically generated sound: recent advances in rotor noise prediction, AIAA Paper 2000-0345, 2000.
- [35] T. Colonius, J.B. Freund, Application of Lighthill equation to a Mach 1.92 turbulent jet, *AIAA Journal* 38 (2) (2000) 368–370.
- [36] C. Bogey, X. Gloerfelt, C. Bailly, An illustration of the inclusion of sound–flow interactions in Lighthill's equation, Technical Note, *AIAA Journal*, 2003, to appear. See also AIAA Paper 2001-2255.
- [37] X. Zhang, A. Rona, G.M. Lilley, Far-field noise radiation from an unsteady supersonic cavity, AIAA Paper 95-040, 1995.
- [38] N. Curle, The influence of solid boundaries upon aerodynamic sound, *Proceedings of the Royal Society of London A* 231 (1955) 505–514.
- [39] M.E. Goldstein, *Aeroacoustics*, McGraw-Hill, New York, 1976.

- [40] D.P. Lockard, An efficient, two-dimensional implementation of the Ffowcs Williams and Hawkings equation, *Journal of Sound and Vibration* 229 (4) (2000) 897–911.
- [41] Y.P. Guo, Application of the Ffowcs Williams–Hawkings equation to two-dimensional problems, *Journal of Fluid Mechanics* 403 (2000) 201–221.
- [42] A. Powell, Aerodynamic noise and the plane boundary, *Journal of the Acoustical Society of America* 32 (8) (1960) 982–990.
- [43] G.R. Kirchhoff, Towards a theory of light rays, *Annalen der Physik und Chemie* 18 (1883) 663–695.
- [44] K.S. Brentner, F. Farassat, An analytical comparison of the acoustic analogy and Kirchhoff formulation for moving surfaces, *AIAA Journal* 36 (8) (1998) 1379–1386.
- [45] B.A. Singer, K.S. Brentner, D.P. Lockard, G.M. Lilley, Simulation of acoustic scattering from a trailing edge, *Journal of Sound and Vibration* 230 (3) (2000) 541–560.
- [46] P. di Francescantonio, A new boundary integral formulation for the prediction of sound radiation, *Journal of Sound and Vibration* 202 (4) (1997) 491–509.
- [47] J. Prieur, G. Rahier, Comparison of Ffowcs Williams–Hawkings and Kirchhoff rotor noise calculations, *AIAA Paper* 98-2376, 1998.
- [48] X. Gloerfelt, C. Bogey, C. Bailly, D. Juvé, Aerodynamic noise induced by laminar and turbulent boundary layers over rectangular cavities, *AIAA Paper* 2002-2349, 2002.